RESEARCH ARTICLE

An examination of the nature of global MODIS cloud regimes

Lazaros Oreopoulos[1], Nayeong Cho[1,2], Dongmin Lee[1,3], Seiji Kato[4], and George J. Huffman[1]

[1]NASA-GSFC, Earth Science Division, Greenbelt, Maryland, USA, [2]USRA, Columbia, Maryland, USA, [3]GESTAR, Morgan State University, Baltimore, Maryland, USA, [4]NASA-LARC, Climate Science Branch, Hampton, Virginia, USA

Abstract We introduce global cloud regimes (previously also referred to as "weather states") derived from cloud retrievals that use measurements by the Moderate Resolution Imaging Spectroradiometer (MODIS) instrument aboard the Aqua and Terra satellites. The regimes are obtained by applying clustering analysis on joint histograms of retrieved cloud top pressure and cloud optical thickness. By employing a compositing approach on data sets from satellites and other sources, we examine regime structural and thermodynamical characteristics. We establish that the MODIS cloud regimes tend to form in distinct dynamical and thermodynamical environments and have diverse profiles of cloud fraction and water content. When compositing radiative fluxes from the Clouds and the Earth's Radiant Energy System instrument and surface precipitation from the Global Precipitation Climatology Project, we find that regimes with a radiative warming effect on the atmosphere also produce the largest implied latent heat. Taken as a whole, the results of the study corroborate the usefulness of the cloud regime concept, reaffirm the fundamental nature of the regimes as appropriate building blocks for cloud system classification, clarify their association with standard cloud types, and underscore their distinct radiative and hydrological signatures.

1. Introduction

The role of clouds in the Earth's water and energy cycle cannot be overstated. Atmospheric heating rates (due to radiative and phase change processes), surface energy budgets (radiative and turbulent), and precipitation rates depend strongly on cloud coverage, optical and microphysical properties, and frequency of occurrence. Cloud impacts are often studied either collectively or by employing only rudimentary classification, e.g., based on phase (liquid and ice clouds) or height (low, middle, and high clouds). However, as we will show here, a more methodical categorization of the multitude of observed cloud systems can potentially be far more useful and serve as a springboard of advanced physically based diagnostics to evaluate cloud processes in global climate model (GCM) simulations.

There has recently been a proliferation of studies focusing on the subject of systematic identification of distinct cloud regimes via extraction of patterns in the covariation of cloud vertical location and extinction. A common practice is to deduce the patterns using clustering techniques [*Jakob and Tselioudis*, 2003; *Rossow et al.*, 2005; *Zhang et al.*, 2007]. The search for patterns can be performed on either discrete geographical regions or climatic zones [e.g., *Jakob and Tselioudis*, 2003; *Haynes et al.*, 2011; *Oreopoulos and Rossow*, 2011; *Tan and Jakob*, 2013] or encompass global scales [*Tselioudis et al.*, 2013]. Once the regimes have been identified, major features such as frequency of occurrence and distributions of cloud fraction, top and base height, vertical structure, optical properties, etc., can be inferred, depending on the availability of coincident observations. These features can in turn serve as the basis for more advanced analysis such as evaluation of cloud regime role in weather and climate processes.

One of the earlier works embracing the cloud regime concept was that by *Jakob et al.* [2005]. The authors investigated the radiative (surface and top of the atmosphere (TOA) fluxes), cloud property (profiles of cloud fraction, joint variations of cloud height, and vertical extent), thermodynamical (columnar water vapor, temperature profiles), and dynamical (vertical velocities) characteristics of International Satellite Cloud Climatology Project (ISCCP) cloud regimes in the western Pacific in order to better understand the role of clouds on regional water and energy budgets. Later, *Jakob and Schumacher* [2008] brought in precipitation and latent heating data from the Tropical Rainfall Measuring Mission precipitation radar in the same region to successfully associate cloud regimes with three major precipitation regimes of distinct rainfall rates and latent heat profile characteristics. *Gordon and Norris* [2010] investigated whether particular midlatitude

oceanic cloud regimes, as derived by their own in-house cluster analysis of ISCCP cloud optical thickness and cloud top pressure 2-D histograms, were associated with systematic deviations from the mean atmospheric state as represented by reanalysis fields of relative humidity, temperature, vertical velocity, and horizontal temperature advection.

The ISCCP project has been providing for a few years now its own cloud regime ("weather state," in their terminology) product based on application of a *k*-means clustering algorithm [*Anderberg*, 1973] on cloud optical thickness–cloud top pressure 3 h joint histograms of 2.5° gridcells (http://isccp.giss.nasa.gov/climanal5.html). The initial edition of the data set was available only for the deep tropics (15°S to 15°N) [*Rossow et al.*, 2005] but was subsequently expanded to cover three distinct geographical zones (extended tropics, 35°S to 35°N, and northern and southern midlatitudes between 30° and 65°). Compositing radiative flux and precipitation data by ISCCP weather state led to insight on their hydrological and radiative nature [*Haynes et al.*, 2011; *Oreopoulos and Rossow*, 2011; *Lee et al.*, 2013; *Rossow et al.*, 2013] and, in particular, to a better understanding of their individual importance to the water and energy budget as measured by contribution strength. At the same time, parallel efforts concentrated on deriving regimes from appropriately equipped GCMs, with comparisons to observed regimes and attribution of potential cloud radiative feedbacks as two notable lines of research [*Williams and Tselioudis*, 2007; *Williams and Webb*, 2009]. Other novel applications have also started to emerge recently such as examination of aerosol indirect effect dependence on regime type and transitions, as recently attempted by *Gryspeerdt and Stier* [2012] and *Gryspeerdt et al.* [2014] in the tropics using Moderate Resolution Imaging Spectroradiometer (MODIS) data.

Recently, *Tselioudis et al.* [2013] successfully completed the inexorable last step of deriving a single set of ISCCP weather states for the entire globe. These investigators then used vertical cloud structure information from combined CloudSat-CALIPSO data to deduce the mean vertical layering of weather state cloud fields and reanalysis data of vertical pressure velocity to obtain clues about the dynamical environment within which they form. Their analysis demonstrated that the vertical layering of the various states is unique and that the mean vertical motion of their environment follows an expected progression from intense ascent to gentle descent as one transitions from more to less vertically developed states.

The present paper introduces a new set of global cloud regimes derived by employing clustering analysis on daily joint histograms from multiyear passive cloud retrievals by the MODIS instrument aboard the Terra and Aqua satellites. MODIS-based regimes using the same or similar clustering methodology have been derived previously [*Williams and Webb*, 2009; *Lebsock et al.*, 2010; *Gryspeerdt and Stier*, 2012; *Gryspeerdt et al.*, 2014], but this is the first that employs the longest data set available to date and is truly global, which makes it the most comparable to its ISCCP counterpart in *Tselioudis et al.* [2013]. Our goal is twofold: first, to reaffirm that the regime concept is as robust as suggested by the prior ISCCP-centric work and can therefore serve as the cornerstone for cloud system classification in observations and models, and second, to support the notion that other coincident observations help advance our understanding of the nature of cloud mixtures mapped into regimes. The latter objective becomes particularly important if one wants to determine their distinct hydrological and energetic characteristics, invaluable information for assessing the realism of cloud simulations in climate models.

2. Data Sources

2.1. MODIS Cloud Properties

To derive the MODIS cloud regimes (hereafter CRs, details are forthcoming in section 3.1) we use 10 years (July 2002 to June 2012) of daily Level-3 (D3) 1° ISCCP-like joint histograms of cloud optical thickness (τ) and cloud top pressure (p_c) from MODIS-Aqua (MYD08_D3 data set, Collection 5.1) and MODIS-Terra (MOD08_D3, Collection 5.1). The joint histograms are generated from all MODIS pixels for which cloud retrievals are possible and successful, without regard for cloud phase, i.e., pixel count contributions in these histograms come from both liquid and ice (and a few undetermined phase) cloud retrievals. Since τ can be retrieved from MODIS measurements only during sunlit hours, the joint histograms are only available during daytime. The ISCCP-like MODIS joint histograms originally consisted of seven τ bins and seven p_c bins, but we combined the first two τ bins into one (extending from 0 to 1.3) for a total of 42 bins (cf. Figure 1) with the exact same boundaries (note, however, that for MODIS, the actual upper limit of τ is 100) as those of the ISCCP histograms used for that project's "weather state" analysis [*Rossow et al.*, 2005; *Oreopoulos and Rossow*, 2011; *Tselioudis et al.*, 2013].
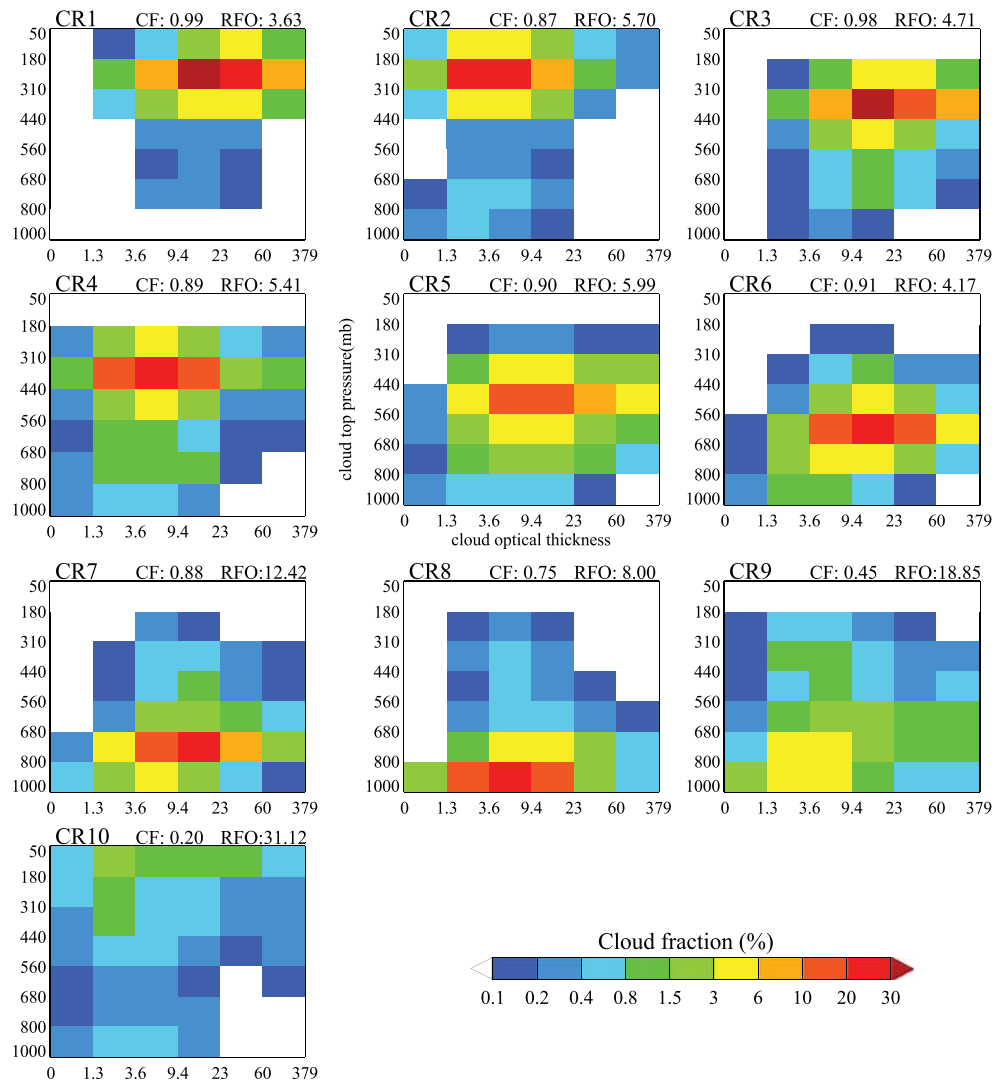
Figure 1. The cloud regime centroids as derived from *k*-means clustering analysis on the combined Aqua-Terra MODIS 1° joint p_C-τ histograms. We show for each regime the multiannual globally averaged relative frequency of occurrence (RFO) and the mean total cloud fraction derived from compositing MODIS total cloud fractions of successful retrievals CF$_S$ as in Figure 3.

In addition to the joint histograms, for compositing purposes we also use several gridded mean quantities available in the MODIS D3 data sets. These quantities are the mean cloud fraction and mean τ of successful cloud retrievals (total, as well as phase-dependent, for both variables). While the phase-agnostic versions of these variables can also be obtained from the p_C-τ joint histogram, we chose for simplicity and for the purposes of making an independent consistency check to use the mean quantities provided independently. As will be shown shortly, performing separate compositing for these two variables provides further insight into the cloud types (as perceived by passive measurements, at least) that contribute to the makeup of the MODIS CRs.

2.2. A-Train Data

2.2.1. CALIPSO-CloudSat-CERES-MODIS Product

An enhanced perspective on the nature of cloud regimes can be achieved by employing cloud retrievals from coincident active measurements, as sampled, combined, and gridded within the CALIPSO-CloudSat-CERES-MODIS (CCCM or C3M) product [*Kato et al.*, 2010, 2011]. This product was conceived as an aggregator and integrator of measurements from the Cloud-Aerosol Lidar and Infrared Pathfinder Satellite Observations (CALIPSO) Cloud-Aerosol Lidar with Orthogonal Polarization (CALIOP), CloudSat Cloud Profiling Radar (CPR),

Clouds and the Earth's Radiant Energy System (CERES), and MODIS (from the Aqua satellite in the case of the latter two instruments). The mapping strategy of C3M is to match cloud and aerosol properties from CALIOP (nominally resolved at 0.33 km) and cloud properties from the CPR (nominally resolved at 1.4 km) to a MODIS pixel (1 km) and then to the CERES footprint (approximately 20 km) with the highest CALIPSO and CloudSat ground track coverage. Each C3M granule contains 24 h of data, and for the purposes of compositing the variables of interest by CR, we select only the data subset that falls within 1° D3 gridcells with an Aqua CR occurrence for that day.

Our compositing analysis uses 4 years (2007–2010) of C3M data for the following variables: (a) *Cloud layer top level height* (CCCM-13), the vertical location where the cloud top starts according to combined CloudSat and CALIPSO retrievals. (b) *Cloud layer base level height* (CCCM-15), also based on CloudSat and CALIPSO, the vertical location of the first cloud-free layer below a profile's cloud layer. (c) *Cloud fraction profile* (CCCM-52), the volumetric cloud fraction vertical profile derived from CALIPSO and CloudSat data (assigned to CALIPSO bins) and defined as the ratio of CALIPSO cloudy bins within a layer (as delineated by the radiative transfer model used to obtain irradiance profiles), to the total number of bins within the same layer. (d) *CloudSat cloud type* (CCCM-73), the cloud type according to CloudSat's 2B-CLDCLASS mask [*Sassen and Wang*, 2008] provided as the ratio of layers with a given cloud type divided by total number of cloud layers. The CloudSat cloud types are cirrus (Ci), altostratus (As), altocumulus (Ac), stratus (St), stratocumulus (Sc), cumulus (Cu), nimbostratus (Ns), and deep convective clouds (Cb). In practice, the St cloud type, as defined by the 2B-CLDCLASS, occurs very rarely. (e) *Liquid water content (LWC) profile* (CCCM-85), the liquid water content vertical profile used for radiative flux computations. (f) *Ice water content (IWC) profile (CCCM-86)*, the ice water content vertical profile used for radiative flux computations. The sum of the vertically integrated LWC and IWC from CALIPSO and CloudSat retrievals is renormalized based on MODIS cloud optical thickness values. Both water content profiles are averaged over the cloudy part of the CERES footprint only.

2.2.2. Atmospheric Infrared Sounder Level-3 Profiles

To gain a better understanding of the thermodynamical environment in the vicinity of MODIS Aqua cloud regimes, we employ temperature and water vapor profiles derived from Aqua's AIRS (Atmospheric Infrared Sounder) instrument. Specifically, we use daily AIRS Level-3 Version 6 daytime (ascending node) air temperature and relative humidity profile products generated from the aggregation on a 1° grid of individual AIRS L2 swath air temperature and relative humidity profiles. Air temperature is resolved vertically into the 24 World Meteorological Organization (WMO) standard pressure levels from 1000 to 1 hPa, while relative humidity is presented on a coarser grid, namely, 12 WMO standard levels from 1000 to 100 hPa. The data used here extend 9 years, 2003–2011.

As pointed out by *Tian et al.* [2013] and others before, an infrared instrument like AIRS has reduced sensitivity to air temperature and water vapor near and below clouds, so in areas where spatially extensive and optically thick CRs occur, AIRS-only coverage is potentially more limited and results in spatial sampling biases. Some relief comes from incorporating into the retrieval algorithm the optically transparent microwave frequencies of the Advance Microwave Sounding Unit (AMSU), which make possible the retrieval of air temperature and (to a lesser extent) humidity profiles for an infrared effective cloud fraction (i.e., the product of emissivity and cloud fraction) up to about 70%. At larger effective cloud fractions, however, rapid decreases in the number of high-quality retrievals become unavoidable [*Tian et al.*, 2013]. In general, it is expected that cloud-induced sampling effects will be more evident in the AIRS humidity than the temperature product [*Tian et al.*, 2013]. Given these potential sampling biases, we supplement the temperature and humidity compositing analysis with additional sources of data described in the next subsection.

2.3. Reanalysis Data

Considering the uncertainties of AIRS temperature and humidity retrievals in the vicinity of near-overcast CRs, a compositing of these variables by MODIS CR is also performed using NASA's Modern Era Retrospective analysis for Research and Applications (MERRA) [*Rienecker et al.*, 2011] data set, produced by version 5.2.0 of the Goddard Earth Observing System atmospheric model and data assimilation system. While MERRA assimilates AIRS data that suffer from the caveats mentioned earlier, assimilation is restricted to only clear-sky and cloud-cleared *radiances* and does not comprise any physical variables retrieved by AIRS algorithms. MERRA also assimilates profiles from other sources such as microwave sounders and radiosondes. The MERRA

profiles of temperature and moisture can therefore be considered quasi-independent from AIRS for these particular variables. As pointed out by *Tian et al.* [2013], no single study exists to quantify the uncertainties of the MERRA tropospheric air temperature and humidity vertical structure, which are expected to be greater (especially for moisture) in locations where they are more heavily skewed toward model values. For the purposes of our study, performing compositing analysis of temperature and humidity profiles with two separate data sources serves as an important consistency check of any systematic relationships that may emerge between specific (anomaly) profile shapes and CRs.

In addition to the temperature and moisture profiles, we also use MERRA's large-scale vertical velocity data, specifically pressure vertical velocity at 500 hPa, in order to explore possible associations with a fundamental indicator of the CRs' dynamical environment.

The MERRA data used here is daily averaged and has 1.25° horizontal resolution and 42 vertical layers (data set "inst3_3d_asm_Cp") from which we use only the lowest 24 layers (up to 10 hPa). The time period spans July 2002 to June 2012, coincident with our MODIS CR availability. Spatial interpolation is used to achieve matching with the 1° grid of the MODIS CRs.

2.4. CERES Gridded Fluxes

For radiative flux (irradiance) compositing, we use CERES SYN1deg-Daily edition 3A "combined" Terra-Aqua radiative fluxes at 1° to derive gridded daily Cloud Radiative Effect (CRE), the difference between all-sky and clear-sky fluxes, at both the top of the atmosphere (TOA) and surface (SFC). The data set spans 10 years, July 2002 to June 2012, same as the CR data set. The CERES SYN1deg products provide CERES-observed temporally interpolated TOA radiative fluxes and coincident MODIS-derived cloud and aerosol properties and include geostationary-derived cloud properties and broadband fluxes that have been carefully normalized with CERES fluxes in order to maintain the CERES calibration. They also contain *computed* unconstrained and constrained (to the CERES-observed TOA fluxes) TOA, in-atmosphere, and SFC fluxes. The computation of these fluxes is achieved with the NASA-Langley version of the Fu-Liou radiative transfer model [*Kato et al.*, 2011]. As input for the computations, geostationary satellite [*Minnis et al.*, 1994] and (NASA-Langley's own) MODIS cloud properties [*Minnis et al.*, 2011] along with atmospheric profiles provided by Goddard Modeling and Assimilation Office reanalysis are used. The computations are performed for conditions that comprise all-sky, cloudless-sky, pristine (cloudless-sky without aerosols), and all-sky without aerosol atmospheric states. Here we use fluxes for only the first two atmospheric states, both at thermal infrared (longwave or LW), and solar (shortwave or SW) wavelengths to calculate respective CREs at the TOA and SFC.

2.5. Global Precipitation Climatology Project Precipitation

Precipitation compositing by CR relies on the Global Precipitation Climatology Project (GPCP) data set, specifically the GPCP One Degree Daily Precipitation Data Set (1DD Data Set) which provides daily, global 1° gridded fields of surface precipitation totals from October 1996 through the delayed present. The 1DD draws upon several different, rather heterogeneous, data sources covering different areas of the globe and extends a significant amount of effort to make the complete end product as homogeneous as possible. The 1DD product merges rain gauge data and measurements from geostationary and polar-orbiting satellites (coming from such diverse instruments such as infrared sensors, microwave imagers, and precipitation radars). These wide-ranging data streams have different strengths and weaknesses (e.g., rain gauges are locally accurate but statistically noisy; infrared sensors aboard geostationary satellites have good coverage, but their measurements only empirically relate to rainfall) that are taken into account to optimize the data merging process. On the whole, the GPCP-1DD product is the longest-running global daily precipitation data set that has been extensively validated [*Adler et al.*, 2001, 2003; *Yin et al.*, 2004].

We use GPCP-1DD version 1.2 daily sums of precipitation amounts (mm/d) covering the period from July 2002 to June 2012 (same period as the CR and CERES data sets). While higher temporal and spatial resolution precipitation data sets exist for the period of MODIS CR availability, such as TMPA-3B42 used in similar work by *Lee et al.* [2013], only GPCP-1DD provides the extensive spatial coverage that makes compositing with the MODIS CRs possible on a full global scale.

3. MODIS Cloud Regimes

3.1. Derivation of Regimes

Following the methodology used to derive ISCCP weather states, we applied the *k*-means clustering algorithm of *Anderberg* [1973], as implemented in the Fortran code available on the ISCCP weather state website, on the global MODIS p_c-τ joint histograms. Since the joint histograms are available only during sunlit hours, the derived CRs are therefore also only available during daytime (the interested reader can check *Tan and Jakob* [2013] for an attempt to bypass this limitation using a revised infrared-based clustering algorithm).

In our effort to derive global MODIS cloud regimes, we used as guidance the methodology and findings of *Tselioudis et al.* [2013] whose global ISCCP weather state data set is an extension of earlier versions that distinguished between barotropic (tropics) and baroclinic (midlatitudes) weather states. We combined the Aqua and Terra daily joint histograms for the entire globe into a single data set and passed it to the Anderberg clustering algorithm. As a starting point in our analysis, we assumed 11 clusters, consistent with the final number of clusters in *Tselioudis et al.* [2013] and applied the tests described therein (algorithm convergence, sensitivity to algorithm initialization, cross correlations between the patterns of the cluster centroids, and dispersion of the vectors from their assigned centroid) to examine whether this particular number of clusters is optimal. The analysis revealed that two of the 11 clusters were too similar in centroid pattern correlation and geographical distribution of regime occurrence and that 10 clusters satisfied much better the uniqueness requirements. We focused on the set that consistently reemerged when using different vectors for the initialization of the algorithm. From these similar solutions we chose the cluster set with the smallest variance sum around each cluster centroid. These cluster centroids (which can also be thought as the "mean" joint histograms of all 2-D histograms belonging to the same cluster), each representing a MODIS "cloud regime," are shown in Figure 1, with global mean cloud fraction (from compositing gridcell total cloud fractions of successful cloud optical property retrievals, as discussed later) and global multiannual relative frequency of occurrence (RFO) provided above each panel. Maps of each regime's multiannual mean RFO are provided in Figure 2. The RFOs for both figures are obtained by normalizing with respect to the total number of gridcells where a cloudy regime occurs, i.e., the clear regime with zero cloud fraction of successful retrievals (about 12% of gridcells) is not accounted for. Taken together, these two figures provide ample demonstration of the distinctiveness of our 10 clusters. The ordering of the regimes is somewhat arbitrary but generally follows the convention first adopted by *Rossow et al.* [2005] to assign indices in order of progressively weaker implied dynamical forcing and cloud amount. A qualitative discussion of the nature of these CRs, based solely on Figures 1 and 2, and the features they may have in common with the ISCCP weather states of *Tselioudis et al.* [2013] follows in the next subsection.

3.2. Comparison With ISCCP Global Weather States

As already mentioned, a realistic qualitative characterization of the MODIS CRs can be made based entirely on the information content in Figures 1 and 2. Further insight on the nature of the CRs will be provided in the presentation of the compositing results, which inevitably sheds additional light. Likewise, the comparison with the ISCCP Weather States (WS) of *Tselioudis et al.* [2013] relies on the examination of their Figures 2 and 3 as well as descriptions in that paper's subsection 3a. An imperfect correspondence should come as no surprise given numerous differences in the data sets. Besides differences in diurnal sampling (twice a day for MODIS versus every 3 h for ISCCP), grid size (1° for MODIS versus 2.5° for ISCCP), and time series length (10 years for MODIS versus 26 years for ISCCP), dissimilar retrieval algorithms [*Pincus et al.*, 2012] are expected to play a major role in creating distinctiveness. MODIS and ISCCP employ different approaches in cloud masking, quality control decisions that determine which pixels are retained for optical property estimation (i.e., the so-called "clear-sky restoral" by MODIS which eliminates many edge pixels; see *Pincus et al.* [2012]), and retrieval of cloud top pressure (especially for high clouds) and cloud optical thickness. Factors involved include pixel size, method of determination of thermodynamic phase, assumptions about cloud single scattering properties, interpretation of partially cloudy pixels, and others. Notably, the clear-sky restoral process employed by the cloud optical property algorithm is unique to MODIS and seems to have a rather substantial impact in many cases on the number of cloudy pixels a 2-D joint histogram contains. We therefore deem informative to contrast in our descriptions below the mean cloud fractions of successful retrievals, CF_s, to the *daytime* cloud fractions from the MODIS cloud mask CF_m (MOD35 product; see *Ackerman et al.* [1998]). According to MOD35, the percentage of gridcells that are entirely clear is only about 3% (from 12%
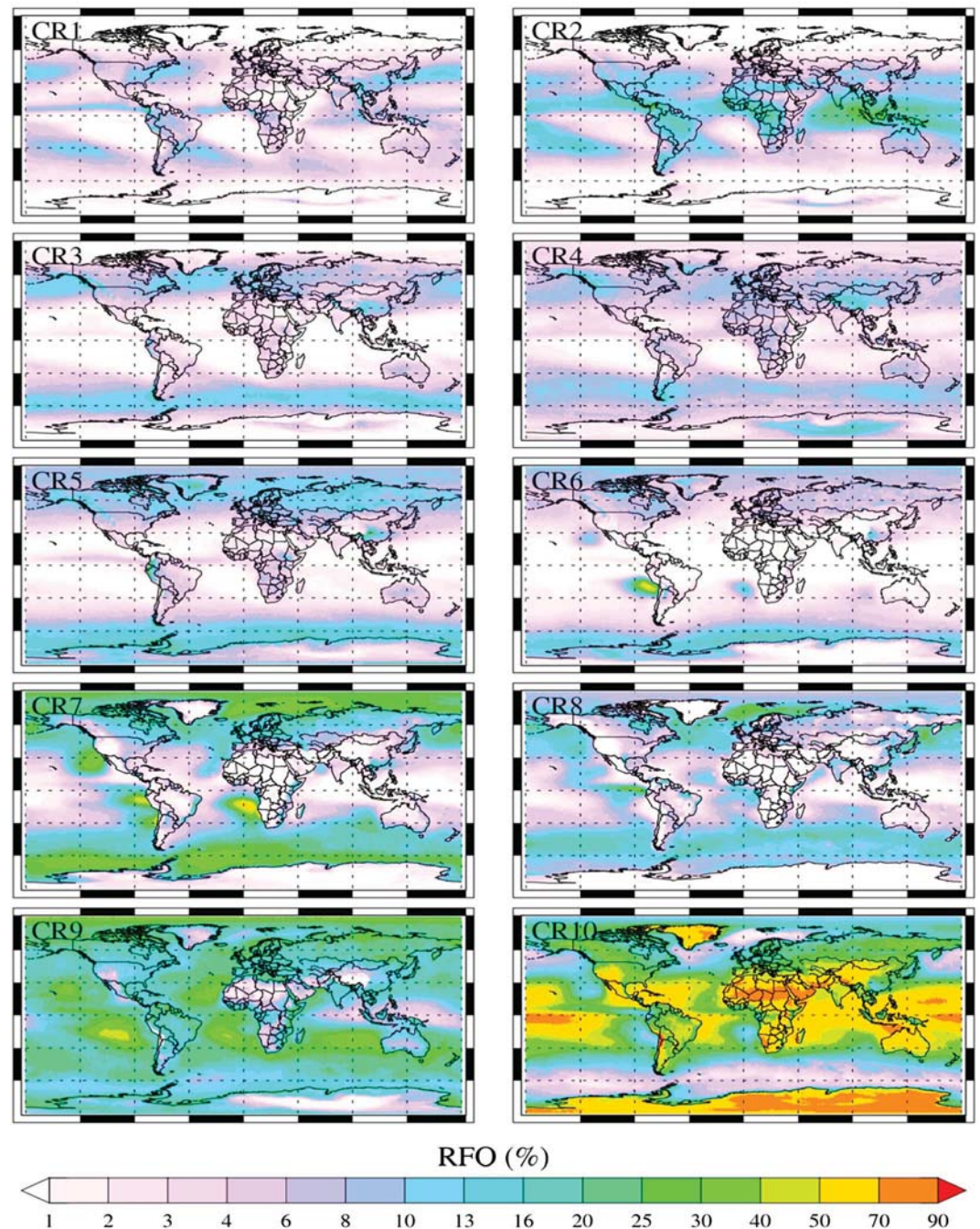
Figure 2. The geographical distribution of the multiyear mean RFO of each MODIS CR from the combined Aqua and Terra data.

implied by the 2-D joint histograms, as stated earlier), similar to ISCCP's 2% [*Tselioudis et al.*, 2013]. For the MODIS clear regime, while $CF_s = 0$ by definition, the cloud mask yields a mean global value $CF_m = 0.09$. Despite approaching cloud retrievals with different philosophies and methodologies, we believe that a first-order comparison between ISCCP and MODIS weather states/cloud regimes is warranted.

MODIS CR1 (RFO = 3.63%; $CF_s = 0.99$; $CF_m = 0.996$) seems to represent tropical and frontal convective storm systems as evidenced by plentiful optically thick high clouds and their geographical distribution. Both the centroid pattern and the map of RFO (despite an apparent larger intrusion of CR1 into the extratropics) indicate that this regime is a close relative of ISCCP's WS1. CR2 (RFO = 5.70%; $CF_s = 0.87$; $CF_m = 0.97$) correlates

very well geographically with CR1 and seems to contain many of the cirrus and anvil outflows of CR1 systems. There is no close analog in the ISCCP WS data set, but it appears that CR2 combines to some extent ISCCP's WS3 and WS6. Note that the MODIS data do not contain the pronounced thin cirrus mode (topmost thinnest bin) of ISCCP's WS6 and that CR2 is one of only two MODIS CRs (the other is CR10) with nonnegligible cloud fractions in that bin. *Marchand et al.* [2010] and *Pincus et al.* [2012] provide possible reasons of why ISCCP retrievals falling in that bin may not always be reliable. CR3 (RFO = 4.71%; CF_s = 0.98; CF_m = 0.99) appears to be largely one of the manifestations of midlatitude frontal systems (containing large amounts of alto-type clouds) and resembles ISCCP WS2 in geographical distribution and centroid pattern, but also, to a certain extent, WS5. CR4 (RFO = 5.41%; CF_s = 0.89; CF_m = 0.96) is likely another manifestation of midlatitude storms, containing their optically thinner portions; it shares some geographical features with ISCCP's WS5, but the similarity is not as great in the centroid pattern. CR5 (RFO = 5.99%; CF_s = 0.90; CF_m = 0.96) is also associated with midlatitude storms, but those are shifted more poleward with peak occurrences of nimbo-type clouds that are not as deep because of the shallower troposphere; in the NH this regime is more frequently encountered over land than over ocean and seems to combine features of ISCCP's WS4 and WS5. CR6 (RFO = 4.17%; CF_s = 0.91; CF_m = 0.96) captures cloud systems that apparently comprise many stratus at various geographical zones, including the thicker portions of marine stratocumulus decks; ISCCP's WS11 seems to be the closest relative. CR7 (RFO = 12.42%; CF_s = 0.88; CF_m = 0.96) apparently also consists frequently of subtropical stratocumulus but extends to middle and high latitude oceans as well. Common features can be found with ISCCP's WS9, WS10, and WS11 but with only the latter having the common feature of presence in the Arctic. CR8 (RFO = 8.00%; CF_s = 0.75; CF_m = 0.90) correlates geographically with CR7 and encompasses the thinner and more broken (note the smaller mean cloud fraction) parts of boundary layer clouds. The centroid pattern matches best ISCCP's WS8, but geographical patterns are quite dissimilar (WS9 offers some common features in that regard). Finally, CR9 (RFO = 18.85%; CF_s = 0.45; CF_m = 0.72) and CR10 (RFO = 31.12%; CF_s = 0.20; CF_m = 0.46) are the more weakly forced cloud regimes, or the expressions of the early/late stages of other CRs, with much smaller cloud fractions than all other regimes. CR9 contains many fair weather clouds spanning all latitudes, but with smaller frequencies of co-occurring high clouds than CR10. These two CRs are by far the most frequent regimes, representing collectively almost exactly half of the available joint histograms and are the most affected by clear-sky restoral. CR10 seems to contain clouds appearing in ISCCP's WS6 and WS7 (which together represent about 40% of ISCCP WS occurrences) but not the lower level thick clouds of WS7 which seem to be part of our CR9. The low thin clouds of the latter regime probably belong to ISCCP's WS8.

4. Nature of Cloud Regimes Revealed by Compositing

The conditional compositing of the various data sets by CR entails the generation of statistics for each variable under consideration from the subset that spatiotemporally coincides with one of the CRs. Because the data being composited have, in general, spatial and temporal resolutions that differ from those of the MODIS CRs, the implementation of the compositing process differs slightly among the various data sets. When notable, these compositing subtleties are noted in the relevant subsections below. In principle, one can either perform separate compositing for Terra and Aqua CR occurrences or treat the regimes identified by joint histograms from both MODIS instruments as two distinct secular observations of a single unified data set, akin to the treatment of 3 h ISCCP weather states.

When the variables being composited come exclusively from A-Train data, it makes sense to employ only Aqua CR occurrences, and this is exactly the treatment we adopt in the analysis that follows. When, however, the variables being composited are only available as daily averaged data, two different compositing methods can be applied. Since each gridcell contains nominally a Terra (morning) and an Aqua (afternoon) regime, we have the option of either assigning the same diurnal value to both regimes, even if they are different or considering only those gridcells for which the two regimes are identical. The latter method obviously reduces the number of samples by a factor that is regime-dependent; the overall percentage of samples turns out to be about 23% of those that we would have used if gridcells were not discriminated based on regime persistence (or approximately 46% of the samples that would be available if data from only one satellite were used in the analysis). A comparison of RFOs provided in Figure 1 and forthcoming Figure 15 indicates that the persistence requirement decreases the relative representation in the reduced gridcell sample of all CRs other than CR7 and CR10, i.e., these two regimes are the most likely to persist during daytime.
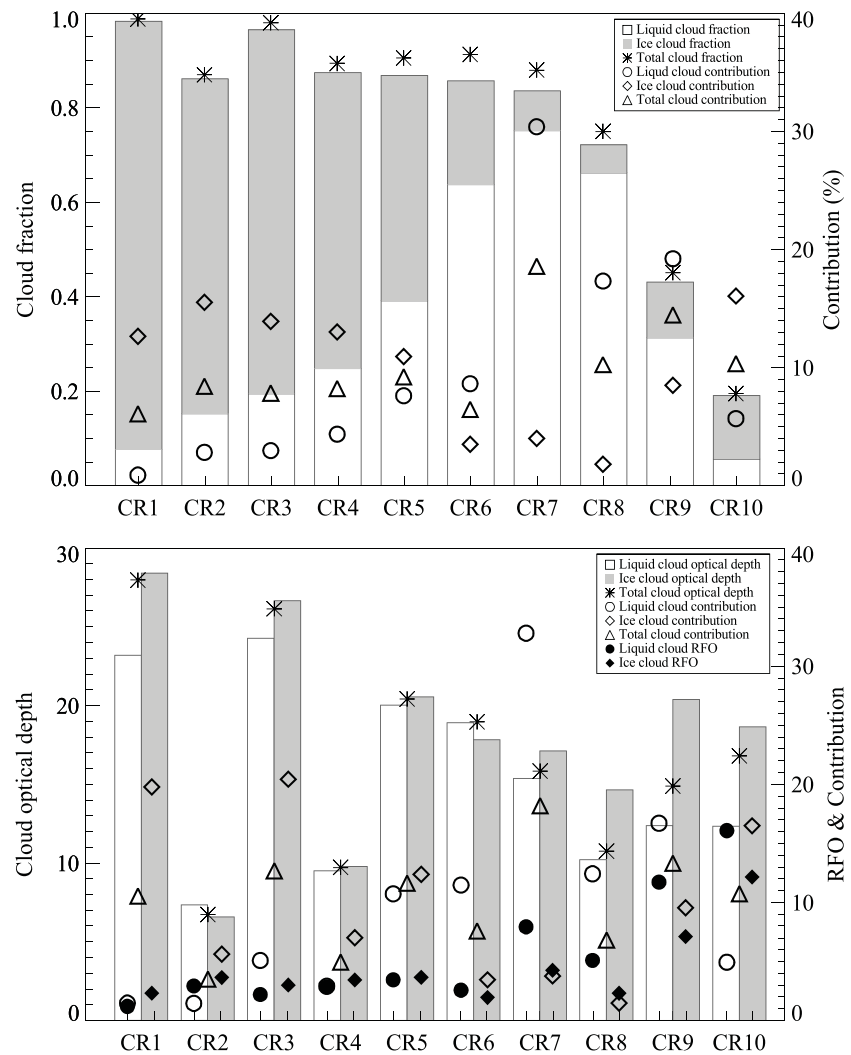
Figure 3. (top) Cloud fraction of successful retrievals CF_s and (bottom) optical thickness means for each MODIS cloud regime derived from compositing. Each panel also shows the respective quantities for clouds identified as being of liquid and ice phase, the global total, as well as phase-dependent RFO, and the percentage contribution of each regime to the overall global mean, for both total and phase-specific quantities. The total cloud fraction exceeds the sum of liquid and ice cloud fractions because of contributions from pixels for which a phase determination was not possible.

The outcomes of the two compositing methods were not very different, and comparing them would have provided only marginal additional insight on the nature of the regimes. Even though it sacrifices sample size, we elected the method that subsamples the gridcells with identical Aqua and Terra regimes because it provides greater consistency in the mapping of regimes to daily averaged observables and ultimately showcases more clearly the distinct nature of the CRs.

4.1. Cloud Properties From MODIS

Figure 3 shows the outcome of compositing MODIS mean gridcell cloud fraction and cloud optical thickness by cloud regime. In addition to total cloud fraction and total cloud optical thickness, compositing was also conducted separately for the corresponding liquid and ice phase quantities. While the total cloud fraction CF_s and optical thickness can in principle be derived from the joint histograms that determine a particular gridcell's assignment to one of the CRs, for simplicity and higher accuracy we used the mean daily averages as provided in the MOD08_D3 (Terra) and MYD08_D3 (Aqua) data sets. The counterpart quantities distinguished by phase cannot be derived from the histograms, so in this case compositing the appropriate 1° daily means of the D3 data sets is mandatory.
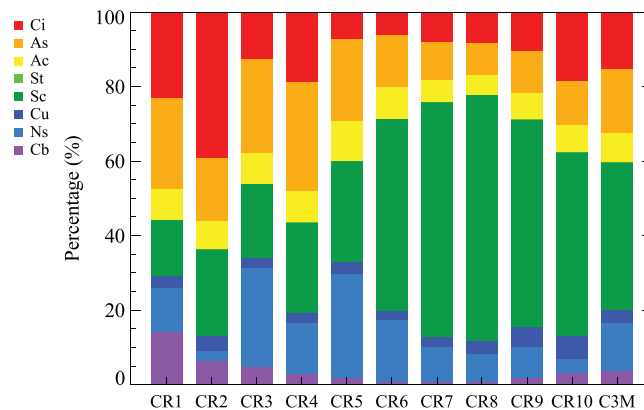
Figure 4. Percentage composition of each Aqua MODIS CR in terms of 2B-CLDCLASS cloud types as recorded in C3M following spatiotemporal colocation and compositing. The last column shows the C3M average across all MODIS Aqua CRs with available colocations.

Figure 3 (top) makes apparent that our CR index assignment convention results in the ratio of ice to liquid cloud fraction to steadily diminish from CR1 to CR8. The ratio rises again for regimes CR9 and CR10 which appear to contain many high/low cloud multilayer situations. Figure 3 (top) also shows the contribution of each CR to the total and individual liquid and ice cloud fraction. We see that CR2 and CR10 are (in roughly equal proportions) the greatest contributors to the total ice fraction, notwithstanding the small, in absolute terms, ice cloud fraction of the latter, which is more than compensated by the large RFO of this regime. The largest contributor to the liquid cloud fraction is CR7 which has the biggest liquid cloud fraction in absolute terms, followed by CR9 whose liquid cloud fraction is less than half of CR7's but exhibits the second largest RFO.

Figure 3 (bottom) shows the total mean τ of each CR as well as its breakdown by phase. It is important to recall here that pixels assigned the ice phase by the MODIS algorithm do not necessarily consist of ice particles throughout the depth of the atmospheric column. Phase determination is greatly affected near-cloud top conditions and is largely agnostic to conditions at the lower levels of a cloud system, so a cloudy column that is deep can consist of ice aloft and of progressively more liquid as one descends closer to cloud base, yet the MODIS phase detection algorithm would still be assigning the pixel to the ice phase.

The optically thickest clouds on average can be found in CR1 and CR3, while the thinnest in CR2 and CR4, for both liquid and ice. The relative importance of the liquid and ice τ in determining total τ depends on the RFO of the two phases: the largest the difference between the two RFOs for a particular CR, the closest the mean total τ is to the τ of the dominant phase. As an example, consider CR8, which has a large contrast between the liquid and ice phase RFO: the mean total τ is almost the same as the τ of the dominant liquid phase. Figure 3 (bottom) also shows the contribution of each CR to the phase-dependent global τ. This contribution is the joint outcome of mean τ values, cloud fraction, and RFO. Case in point, CR10 contributes strongly to the global ice τ because of large RFO and moderately high values of ice τ, despite low values of ice cloud fraction. The contribution to the global liquid τ on the other hand is much more muted even if the RFO of the liquid phase remains strong: the reason is that for this particular CR the relatively weak value of mean liquid τ combines with an extremely weak liquid cloud fraction (Figure 3 (top)). CR1 and CR3 contribute about ~40% to the global ice τ, despite an overall combined RFO < 10%, because their mean ice τ's are large (above 25) and so are their ice cloud fractions.

4.2. Association With CloudSat Cloud Types

Figure 4 sheds further light on the composition of the MODIS CRs (from Aqua in this particular case) by providing their breakdown in terms of "traditional" cloud types. Cloud types in C3M come from CloudSat's 2B-CLDCLASS product (at the time of this writing the latest available version of C3M had not yet incorporated the more recent 2B-CLDCLASS-LIDAR product which adds CALIPSO data in the cloud type classification algorithm). The results of Figure 4 largely support our description of the cloud regimes in section 3.2 which was based solely on the shape of each regime's centroid and the geographical patterns of the regime RFOs.

Given the virtual absence of any St in 2B-CLDCLASS, the most frequent low-level cloud is Sc, which is by far the most dominant cloud type of CR6-10. The apparent strong presence of convection in CR1 is confirmed by the largest fraction of "deep convective" Cb clouds, while the ample existence of anvil/convective
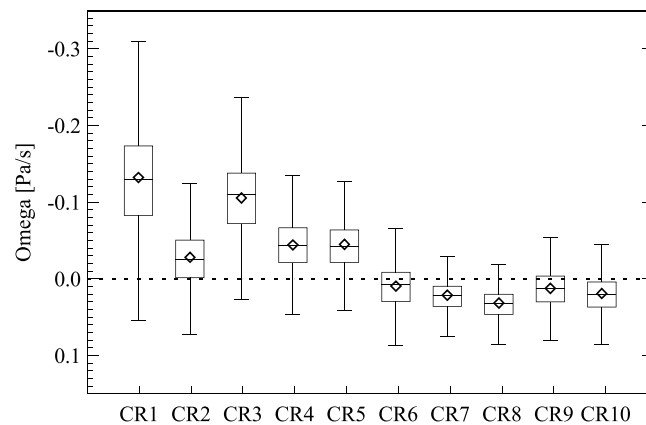
Figure 5. MERRA diurnally averaged vertical motion at 500 hPa composited by MODIS CR. Shown are median (horizontal line), mean (diamond symbol), interquartile range (box), and extreme data point within 1.5 times of the interquartile range (whiskers); the dashed horizontal line separates ascending (negative values) from descending motion.

outflow in CR2 is affirmed by the largest fraction of Ci clouds among all regimes (recall that this regime was shown in Figure 3 to have the lowest mean optical thickness). The largest fraction of Ns clouds, signifying association with midlatitude storms, can be found in CR3 and CR5, consistent with our earlier description based solely on centroid appearance and the preferred geographical locations of the regime. Note that the proportion of what 2B-CLDCLASS calls As does not vary much by MODIS CR, but when accounting collectively for traditional midtroposphere clouds, namely, As and Ac, CR1, CR3, and CR4 distinguish themselves as the regimes containing most of these cloud types, followed closely by CR5. The regimes with the rarest occurrences of intense convection (smallest Cb fraction), according to 2B-CLDCLASS, are CR6-9, which, as we will show later (Figure 15), also happen to be the weakest precipitation producers.

4.3. Vertical Motion and Atmospheric Structure

When compositing MERRA large-scale vertical motion (as expressed by pressure velocity at 500 hPa), as in Figure 5, a clear separation is achieved between regimes in ascending motion areas (negative mean or median pressure vertical velocity), namely, CR1-CR5, and regimes in areas of prevailing descending large-scale motion, namely, CR7-10. CR6 can be thought of as the "separator" regime between these two groups, with mean and median vertical velocity falling almost exactly on the zero line. This figure indicates that CR1 and CR3 occur in the areas of strongest vertical ascent and are quite distinct from the other CRs associated with ascending motion. These results also confirm the appropriateness of seeking connections between
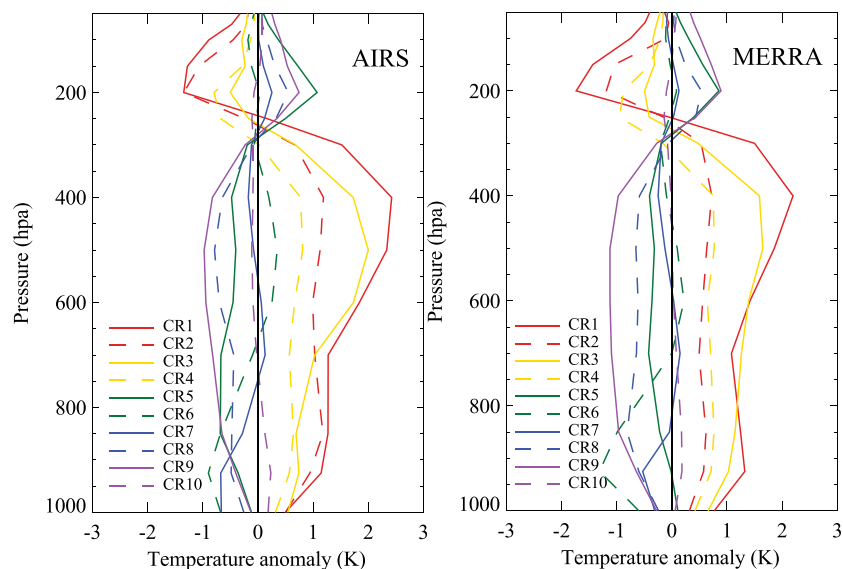

Figure 6. (left) Composites of temperature anomalies for each MODIS-Aqua CR occurrence calculated from daytime AIRS L3 data as described in the text; (right) similar to Figure 6 (left), but using MERRA daily averaged temperature profiles composited for gridcells where Terra and Aqua CRs are identical.
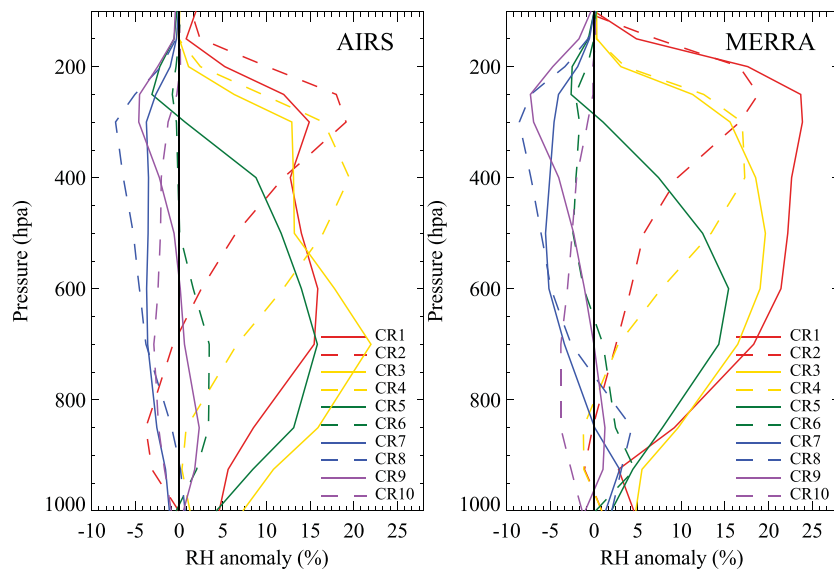
Figure 7. As in Figure 6 but for relative humidity anomalies.

cloud regimes and meteorological conditions (vindicating thus the use of the term "weather states" in prior literature and the corresponding ISCCP product) and the skill of our empirical CR index assignment scheme which did not benefit from information other than the centroid patterns and the geographical distribution of the annual mean RFO.

Composites of temperature and relative humidity (RH) anomalies for AIRS were derived by calculating the difference between individual daytime gridcell profiles and the multiyear monthly daytime mean for that gridcell, sorting the differences by CR, and then grand averaging all available gridcell values. This procedure is very similar to that of *Gordon and Norris* [2010] and was also followed for the daily profiles from MERRA. The composites by CR of temperature anomalies are shown in Figure 6, while those for RH anomalies are shown in Figure 7. The AIRS panel in these two figures is based on Aqua CR occurrences only, while the MERRA panel uses both Terra and Aqua CRs, making an anomaly profile assignment only when an identical CR is identified in the gridcell by both instruments, as explained earlier.

Both temperature and humidity anomalies are well separated by CR. CR1–4, the regimes of radiative warming and greatest implied latent heat warming, as will be shown later, reside in an environment which is warmer than average in the lower and middle troposphere and colder in the upper troposphere and stratosphere. The opposite is true for CR5, CR8, and CR9. CR7 and CR10 (the latter being the most frequent regime) tend to occur under temperature conditions that do not deviate much from gridcell climatology. CR6 seems to form in environments that are colder than average only in the lower troposphere. These findings are quite consistent for both AIRS and MERRA.

RH anomalies (Figure 7) confirm what can be gleaned about regime structure solely from the joint histograms representing CR centroids in Figure 1. The regimes associated with a more active dynamical environment, higher overall cloud fractions, and larger portions of high clouds (CR1–5) stand out by virtue of their high positive RH anomalies and peaks thereof in the middle and upper troposphere. For these regimes the peaks are often near the levels where the joint histograms also exhibit their highest values (this behavior can be more clearly discerned in the MERRA plots). The regimes in weaker dynamical forcing conditions and copious amount of low clouds (CR6-9) have, on the other hand, only modest positive RH anomalies at low altitudes and are characterized by drier than average conditions aloft. CR10, the most frequent and (by far) lowest cloud fraction regime, seems to exist when conditions are drier than average and can be seen to never cross to the positive anomaly side for either data set. This fact along with the low mean cloud fraction would suggest that using the term "fair weather" to describe this regime would have been justified, were it not for its nonnegligible precipitation shown later and the large discrepancy between CF_s and CF_m, which implies that deviations from fair weather conditions are not unusual.
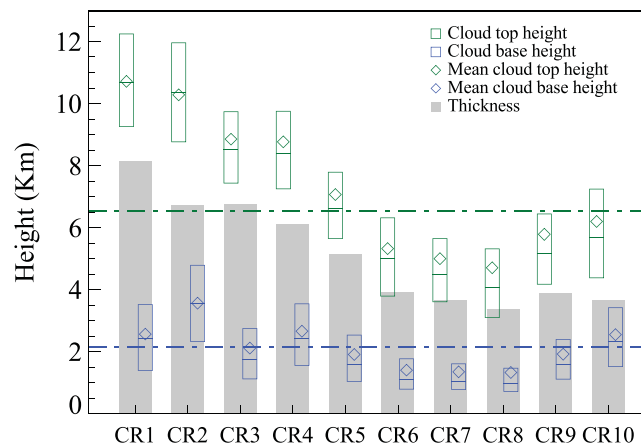
Figure 8. Composites by MODIS-Aqua CR of maximum cloud top height and minimum cloud base height from the C3M data set for the period 2007–2010. The boxes indicate the interquartile range of the respective variables, the horizontal line within each box represents the median, and the diamond symbols the mean. The gray bars are a measure of regime mean (maximum) geometrical thickness and are obtained by simply taking the difference between cloud top and bottom height means.

4.4. Regime Vertical Cloud Structure Assisted by Active Observations

The p_c-τ patterns of the centroids defining the cloud regimes are useful but ultimately flawed indicators of the vertical location and fraction of clouds that dominate each regime. Cloud passive retrievals by nature are limited when it comes to cloud vertical location determination of fully or partially obscured cloud layers in multilayer systems. Such retrievals are, on the other hand, feasible in certain cases from active sensors such as CALIOP and CPR. CALIPSO and CloudSat cloud vertical location indicators are included in C3M, something we take advantage of to obtain glimpses of the active observations' own interpretation of regime vertical structure.

We first show statistics of the vertical location of cloud boundaries in Figure 8. Composite statistical quantities are plotted for each Aqua CR's *maximum* cloud top height and *minimum* cloud base as provided by the C3M data set for the period 2007–2010. The boxes convey the interquartile range of the respective variables, with the horizontal line within each box representing the median and the diamond symbols the mean. A measure of regime mean maximum physical thickness is obtained by simply taking the difference between (maximum) cloud top and (minimum) bottom height means (i.e., the difference between the values represented by diamonds) and is shown as gray bars. Dash-dotted green and blue horizontal lines provide the overall top and bottom mean values averaged across all CRs. Consistent with centroid histogram peaks (cf. Figure 1), CR1–5 exhibit above average top heights, progressively decreasing from CR1 to CR5. Regimes with high proportions of low clouds (CR6–8) appear in Figure 8 to be assigned below average mean cloud top heights by the active instruments. Maximum average cloud top locations rise again toward mean values for CR9 and 10, regimes in which high clouds have sizeable representations. Joint histograms such as that for the CR5 centroid with peak cloud fractions in the middle troposphere are usually viewed with suspicion when coming from passive measurements because of situations where high thin clouds overlapping low thick clouds being often mislabeled as single-layer midlevel clouds. Yet Figure 8 shows that the mean maximum cloud top height of CR5 is indeed close to midtroposphere heights according to the active sensors.
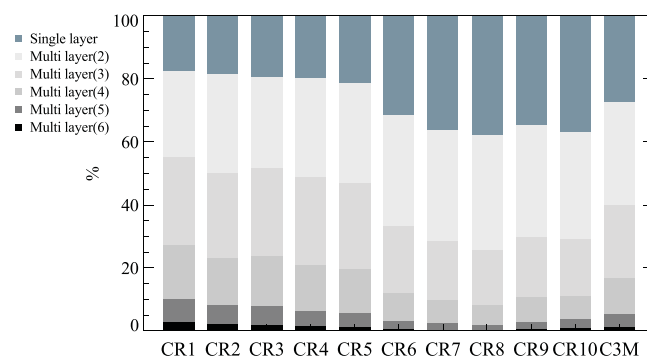

Figure 9. Percent occurrences of a given number of distinct overlapping cloud layers (1–6) per MODIS-Aqua CR according to CloudSat/CALIPSO detections sampled and integrated within the C3M data set during the period 2007–2010.

The more challenging to detect, and therefore probably more uncertain, minimum cloud base heights exhibit less variability than top heights: the individual CR means do not deviate as much from the overall mean, but there is also less variability within the CR as evidenced by the narrower boxes. The end result is that our metric for CR geometrical "thickness" tends to correlate very well with cloud top height, i.e., CRs with the highest cloud tops also appear as geometrically thicker. The highest cloud base unsurprisingly corresponds to CR2, the MODIS regime that encompasses many
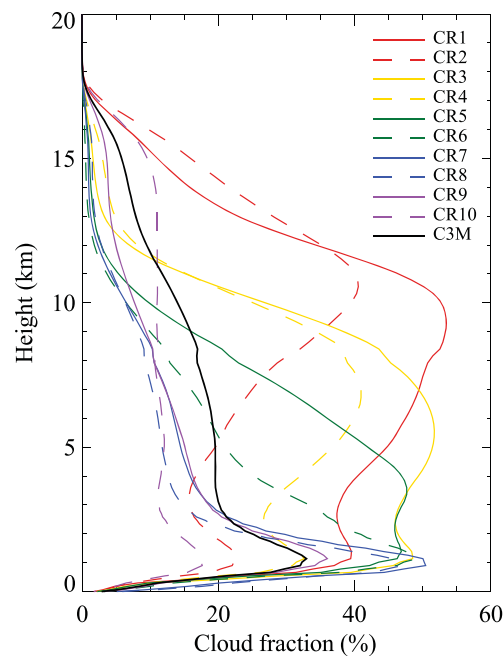
Figure 10. Composites by MODIS-Aqua CR of C3M volumetric cloud fraction profile defined in the text. Also shown is the profile of this quantity averaged across all MODIS-Aqua CRs (curve labeled "C3M").

cirrus and convective anvil outflows. CR6–8 with the lowest cloud tops also have the lowest cloud bases.

While only the lowest and highest layer as detected by CloudSat and CALIPSO were used for Figure 8, one can also examine the total number of distinct cloud layers identified by the conjoint interpretation of the measurements by these satellites. The information conveyed by Figure 9 is simpler than the vertical structure shown for ISCCP weather states by *Tselioudis et al.* [2013] using closely related CloudSat/CALIPSO products. We simply show here how frequently each Aqua CR appears to consist by a given number of distinct cloud layers. Despite its simplicity, the plot bears interesting information. The finding that immediately stands out is that there is clear delineation between regimes with the smallest likelihood of occurrence of a single cloud layer (CR1–5) and those with higher likelihood (CR6–10). CR1 is the regime with the highest likelihood of a complex vertical structure than any other regime, with the greatest chances of 4–6 distinct coexisting cloud layers. While the regimes assigned small indices are more likely to contain more than two distinct cloudy layers, the likelihood of exactly two layers seems to be slightly greater for the low-cloud-dominated
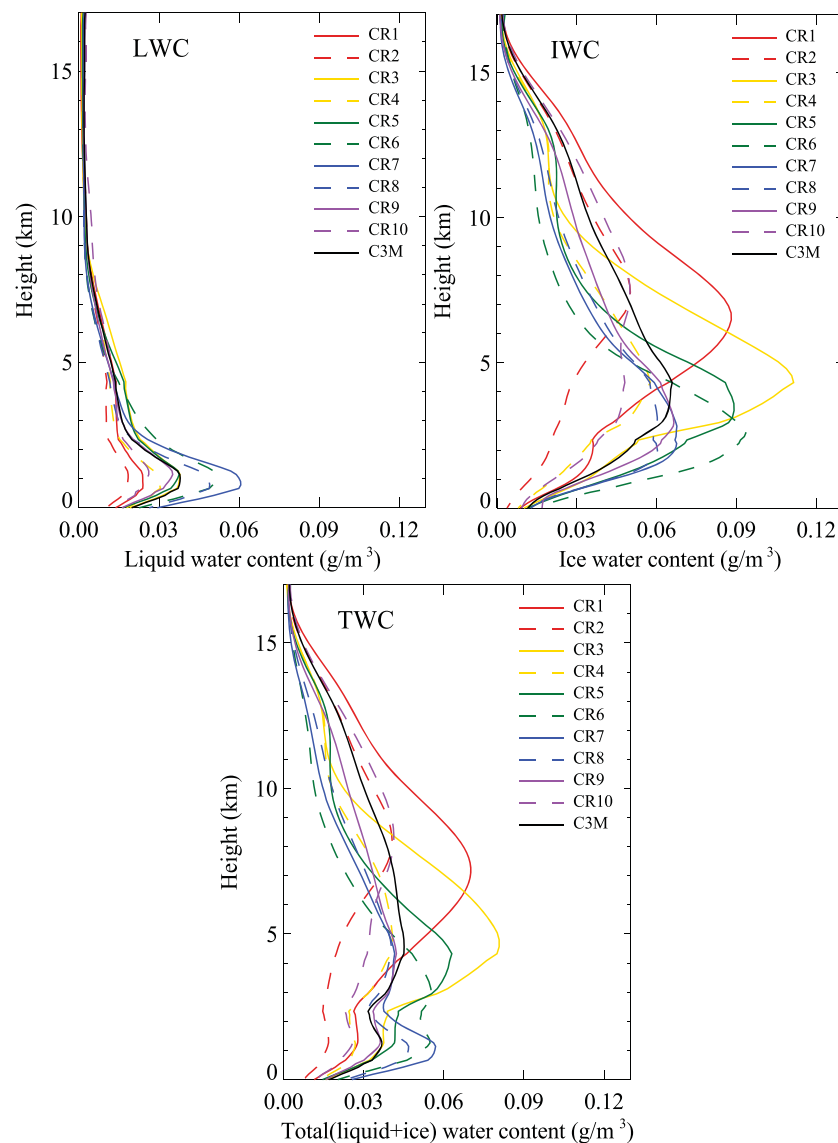
regimes CR6–9, which, however, are also found to more rarely consist of three or more layers compared to CR1–5.

C3M was also used to extract vertical cloud fraction information and create composites for each Aqua regime. C3M contains so-called "volumetric" cloud fraction which is calculated by dividing each layer's cloudy cells by the total (clear and cloudy) number of cells in all valid grid columns contained within a CERES footprint, the reference spatial element used for C3M data sampling and aggregation. Here "layer" refers to one of the (location-dependent) vertical slices in which the atmospheric column is discretized for performing the radiative transfer calculations that produce irradiance profiles within CERES footprints [*Kato et al.*, 2011]. The "cell" vertical size coincides with the resolution of the CALIPSO cloud mask, 30 m and 60 m below and above 8 km, respectively (with the coarser CloudSat mask values being resampled as necessary). Results are shown in Figure 10. Consistency with the joint histograms defining the centroids (Figure 1) can be assessed from two different perspectives: (a) the overall magnitude of volume cloud fraction, a measure of which is the area enclosed by each curve and the ordinate, and (b) the location of the peak volume cloud fraction. The first criterion clearly highlights CR8–10, the regimes of lowest cloud fraction, with CR10's volume cloud fraction remaining around 15% almost throughout the entire troposphere. The second criterion highlights low-cloud-dominated regimes CR6-9 all with volume cloud fraction peaks below 2 km, with the highest altitude peak belonging to CR2 and the next highest peak of CR1. Overall, there is good separation in this plot of "low" regimes CR6–9 and "high" regimes CR1–4, with CR5 delineating the transition.

Another aspect of MODIS CR vertical structure, namely, the variation with height of cloud condensate, is shown in Figure 11. This figure plots composite C3M LWC, IWC, and TWC = LWC + IWC profiles for each Aqua CR, as well as for the entire regime ensemble. These come from modified CloudSat-derived IWC/LWC or CALIPSO-derived IWC/extinction coefficient profiles, scaled by the MODIS total atmospheric column cloud optical thickness and subsequently used to create 600–700 nm extinction coefficient profiles for irradiance profile calculations. The composite LWC profiles have a similar shape for all regimes, but the peak values in the lower troposphere are stronger for the regimes with the most prominent presence of low clouds, i.e., CR6–8. The IWC profiles, on the other hand, which, incidentally, are affected by latitudinal shifts of altitudes where ice can be encountered, are much more varied and intriguing. The highest peak of mean IWC occurs for CR3 and is at a lower altitude than the peak value for CR1 which is second in magnitude, followed closely

Figure 11. Profiles of C3M (top left) LWC, (top right) IWC and (bottom) TWC = LWC + IWC composited by MODIS-Aqua CR. The curve labeled "C3M" is the weighted average of the individual CR curves.

by the peaks for CR5 and CR6. The latter two regimes have substantial proportions of Ns clouds (cf. Figure 4), but since CR6 has collectively fewer Ns, As, Ac, and Ci clouds, its peak IWC is unsurprisingly at a lower altitude. If one ignores particle size variations and any differences arising due to using only Aqua versus combined Aqua-Terra data, the area enclosed by the LWC, IWC, and TWC profiles and the ordinate should be approximately proportional to the liquid, ice, and total optical thicknesses provided in Figure 3, and this is indeed the case. This finding underscores the levels of consistency that can be achieved between coincident passive and active cloud observations.

4.5. Regime Radiative Characteristics

With regard to MODIS CR radiative effects we examine three salient characteristics: the mean diurnal CRE that corresponds to all occurrences of a particular regime, the regime's contribution to the global CRE derived by dividing the sum of all CRE values for a particular regime to the sum of all available CRE values across all regimes, and the CR-dependent contrast between SFC and TOA LW CRE which pertains to atmospheric radiative warming or cooling by clouds in the LW (the counterpart SW relationship is rather trivial as explained by *Oreopoulos and Rossow* [2011] and is therefore not examined here).
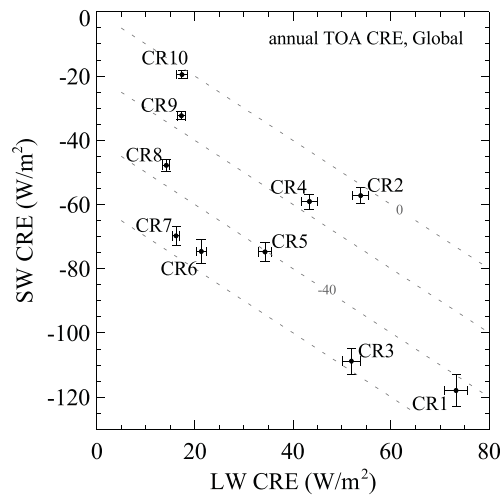
Figure 12. Global mean LW and SW CREs for each MODIS cloud regime. The dashed lines are isolines of constant net CRE. Also included is information about the spatial variability of multiannual mean CRE of each regime which was calculated by taking the standard deviation of all multiannual mean gridcell values, and is shown as horizontal and vertical error bars whose length is one tenth of the standard deviation value. These error bars therefore do not represent the errors to the displayed means which are minute.

The interpretation of the results that follow is aided by recalling that the CRE (SW, LW; TOA, or SFC) can be written as

$$\mathrm{CRE} = A_c(F_{\mathrm{clr}} - F_{\mathrm{ovc}}[f(p_c, \tau)]) \qquad (1)$$

where F_{clr} and F_{ovc} are the cloudless (zero cloud fraction) and overcast (100% cloud fraction) radiative fluxes, A_c is the gridcell total cloud fraction (representing either CF_s or CF_m for the purposes of the discussion here), p_c is the mean cloud pressure (top or bottom), τ is the cloud optical thickness, and f is the function that describes their covariability within the cloudy portion of the gridcell, for example, as a joint probability density function. For fixed F_{clr}, therefore, CRE depends strongly on cloud fraction, cloud opacity as represented by τ (primarily for SW CRE and secondarily for LW CRE), and cloud vertical location as represented by p_c (primarily for LW CRE and to a lesser extent for SW CRE). For fixed cloud conditions, the CRE of course also depends on surface and atmospheric temperatures (for LW), and TOA solar insolation and surface albedo (for SW). One should also recall that when radiative transfer calculations are involved in estimating or adjusting CRE, as in the CERES SYN1deg product used here, the cloud optical property values are not the same as those used to derive the regimes [cf. *Kato et al.*, 2011; *Minnis et al.*, 2011]. Without detailed comparisons on how the optical property distributions differ between the two algorithms for each CR, which is beyond the scope of our study, it remains unknown whether there are any measurable effects on the regime versus CRE mapping presented below.

4.5.1. Regime Mean CRE

We adopt plots similar to those in *Oreopoulos and Rossow* [2011, hereinafter OR11] to summarize regime CREs on a global scale. There is a major difference with the plots of that paper, however: The CREs from CERES being used here to calculate the mean values for each regime do not correspond to fluxes at the nominal time of the regime observation, as in the previous ISCCP analysis, but rather to the diurnal flux averages for the regime's gridcell on that particular day. This makes the SW CREs much smaller in the current analysis than in OR11 since the zero values of the nighttime period are also included in the average.

Figure 12 provides a synopsis of MODIS CR mean global TOA CREs by averaging individual diurnal CREs for each regime. A result that strikes an immediate impression is that no CR exhibits positive mean net CRE, although two regimes, CR2 and CR10, come close. The strongest mean TOA CRE, for both SW and LW comes from CR1, followed in the SW by CR3, which has, however, about the same LW CRE as CR2. These three regimes have the highest proportion of high clouds, some of which can be substantially thick optically. A group of five regimes (CR2 and CR4–7) has similar SW TOA CRE, within ~20 W m^{-2}, but quite a large range of LW TOA CRE, about ~40 W m^{-2} (note that the total SW CRE range across regimes is about 100 W m^{-2}, while the LW CRE range is about 60 W m^{-2}). Note that all regimes in this group have very similar mean total cloud fractions CF_s and CF_m (section 3.2), so the LW TOA CRE diversity comes mainly from vertical location differences of the most common cloud types (cf. Figure 1 and equation (1)).

Regimes dominated by low clouds (CR6–9) exhibit low values of LW TOA CRE (~20 W m^{-2} or below) as expected. CR10, our most prevalent regime, despite being comprised by substantial amounts of high clouds, belongs clearly to the group of weak LW TOA CREs rather than the group of strong values (consisting of CR1-4 and perhaps CR5). Almost certainly, the influence of its high clouds is tempered by its small cloud fraction. Actually, note that the group of regimes closest to the upper left corner of the graph, with the smallest SW and LW TOA CRE effects (CR8–10) comprises the regimes with the smallest cloud fractions, a reminder of the great influence of A_c on CRE magnitude.
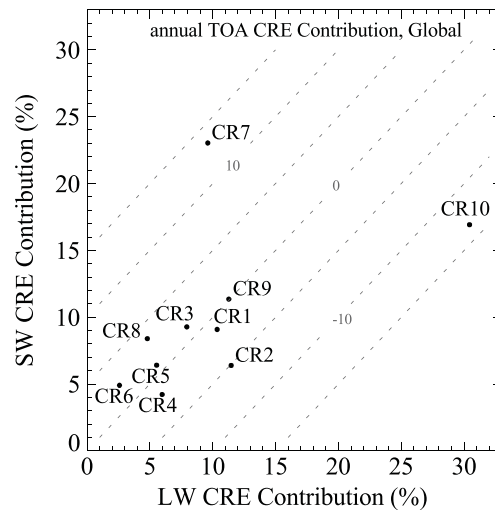
Figure 13. Similar to Figure 12 (without the spatial variability information) but for the percentage contributions of individual cloud regimes to the global LW and SW CRE.

We have also included in this figure information about the spatial variability of multiannual mean CRE of each regime. This was calculated by taking the spatial standard deviation of all multiyear annual mean gridcell values and is included in the graph as horizontal and vertical error bars that represent 1/10th of the actual standard deviation value. These error bars therefore do not represent the errors to the displayed means which are minute. In general, greater mean CRE values also correspond to larger standard deviations. Given the large seasonal and geographical changes of solar insolation, one would expect the SW TOA CRE standard deviations to be much greater than their LW counterparts, but it appears that the absence of a strong hemispherical asymmetry in CR occurrence (on an annual basis at least) dampens the huge solar insolation variance throughout the year, and therefore a great potential contributor to variability of the SW TOA CRE. The values of spatial standard deviation are nonetheless large, indicating that the same CR, depending on specific conditions, can generate a very wide range of CRE responses at least on daily scales, a finding that mirrors OR11 for ISCCP weather states.

4.5.2. Regime Contributions to Global CRE

The mean diurnal CREs of individual CRs provide only one aspect of regime radiative importance. High mean CRE values of a rarely encountered regime may be of small radiative consequence overall, while the opposite can also be true, namely, a regime of relatively modest mean CRE may be an important radiative player if it occurs often. Both scenarios flesh out in the results of Figure 13, which shows the percentage TOA SW and LW CRE contributions of each regime: CR7 and CR10 are the largest contributors to the SW and LW global TOA CRE, respectively, largely because they rank third and first in RFO and not because the global means of their daily values are large. CR9, which has the second largest RFO, is also the second largest SW TOA CRE contributor. The remaining CRs huddle together toward the lower left of Figure 13 with contributions falling within a narrow approximate range of 3–12% for both SW and LW TOA CRE. Within
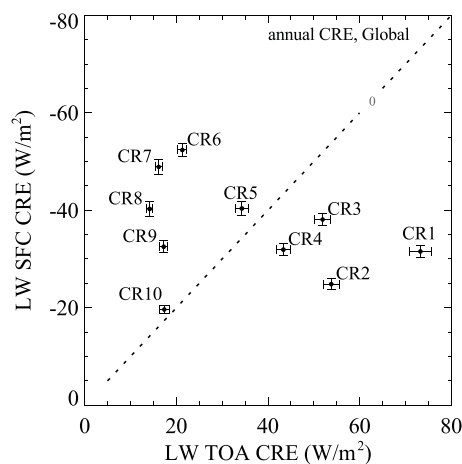

Figure 14. SFC (downwelling) versus TOA (upwelling) mean LW CRE of the various MODIS CRs. Horizontal and vertical error bars have the same meaning as in Figure 12.

that group, one can find CRs with widely different global mean CREs, but almost identical percent contributions: compare for example CR1 and CR8, with equal SW CRE contribution in Figure 13, yet completely different mean diurnal CREs (Figure 12); or, similarly, CR4 and CR8 for LW CRE.

Note that because the net CRE can take (and almost always does) negative values and the global net CRE itself is negative, contributions to this quantity can also be negative. The strongest negative contributions come from CR2 and CR10, the two regimes with near zero global mean net TOA CRE. The physical meaning of the negative net CRE contribution is that a regime reduces in absolute terms the value of the negative net CRE, i.e., it pushes it toward positive values.

4.5.3. TOA Versus Surface LW CRE

Depending on their vertical location, and to a lesser degree, optical properties, clouds either enhance or reduce the overall tendency of the atmosphere to radiatively cool. The weather state concept has proven
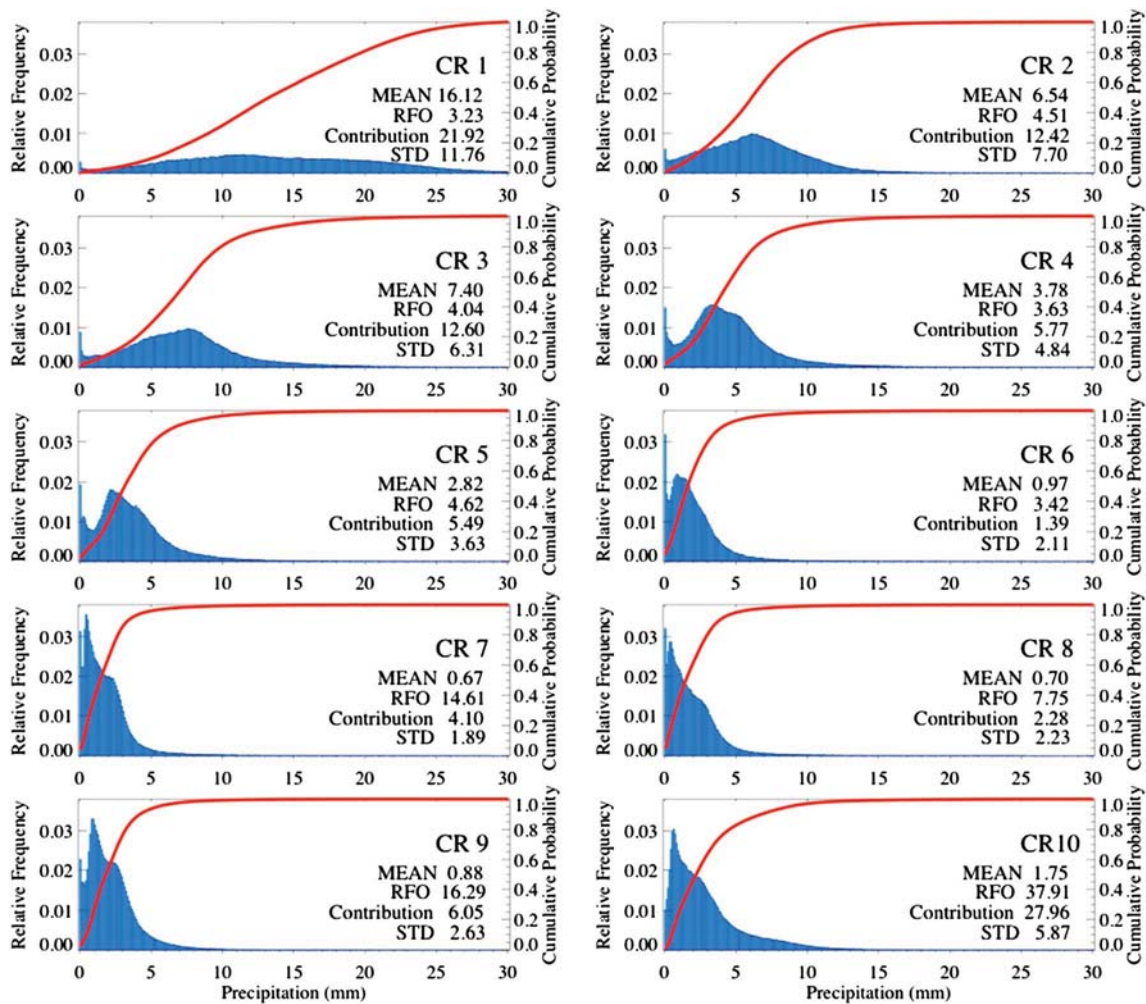
Figure 15. GPCP-based histograms of CR daily precipitation and corresponding cumulative frequency curves (with scale given in the right ordinate). Each panel also shows each CR's mean precipitation rate, its contribution to the global precipitation, the standard deviation of all available gridcell daily values ("STD"), and its RFO. The statistics include zero values of precipitation not shown in the histograms themselves. The RFOs of this figure are different from those of Figure 1 because of the compositing assumptions (i.e., the condition that Aqua and Terra CRs be the same for each gridcell).

successful in past work (OR11) in providing a clear separation between warming and cooling inducing weather states at thermal infrared wavelengths (all CRs due to absorption by cloud particles exhibit a slight warming effect at solar wavelengths, and we therefore do not revisit this trivial result here). As explained in that paper, CRs falling below the diagonal of equal value in a plot of LW SFC CRE versus LW TOA CRE induce radiative warming and those above the diagonal radiative cooling. Figure 14 shows a plot of this type for the MODIS CRs and the CERES-based mean LW CREs. As stated in section 2.4, radiative transfer calculations are involved in deriving the (downwelling flux) SFC CREs, based on NASA-LARC MODIS cloud property retrievals [*Kato et al.*, 2011]. Three groups of cloud regimes emerge from this analysis: CR1–4, with high proportions of high clouds, constitute the group of regimes inducing atmospheric radiative warming, while CR6–8, and to a smaller degree CR9, with prevalence of low clouds constitute the group of regimes inducing radiative cooling. CR5 (many midlevel clouds) and CR10 (mixture of low and high clouds) are close to the line of zero LW CRE divergence (zero LW atmospheric radiative effect). These results are broadly consistent with the ISCCP-based results of OR11 when comparing the CRs/weather states whose centroid patterns look alike. Once again, we have included spatial variability information in the plot as error bars indicating the standard deviation of the gridcell multiyear annual means, similar to Figure 12. The TOA LW CRE error bars are the same as in that figure. The spatial variability of SFC LW CRE is, in general, larger than that of its TOA counterpart for the CRs for which the SFC CRE is larger than the TOA CRE, namely, the low-cloud-dominated CRs to the left of the diagonal.
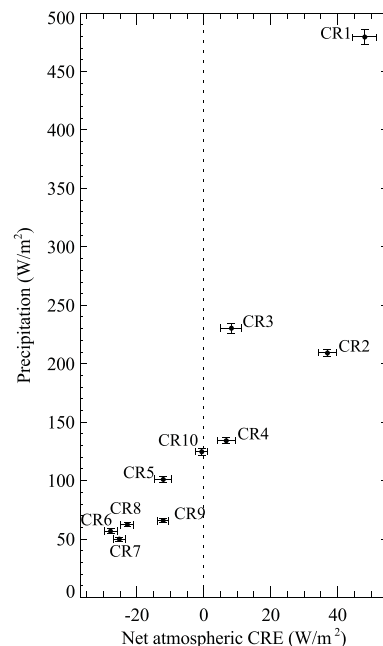
Figure 16. Mean MODIS CR precipitation after conversion to latent heat flux in $W\,m^{-2}$ plotted against the net atmospheric CRE defined by equation (2). The vertical error bars show the spatial standard deviation of gridcell precipitation multiannual means, while the horizontal bars show one tenth of the corresponding quantity for net atmospheric CRE.

4.6. Regime Precipitation Characteristics

A straightforward way to appreciate the different characteristics of precipitation within each regime is to examine precipitation rate frequency histograms and cumulative frequencies for each CR. Once again, we assign a GPCP precipitation rate value only if the Terra and Aqua regimes are identical for a particular gridcell and day. Although not represented in the histograms themselves, zero gridcell precipitation values are accounted for in the statistical metrics shown in each panel.

The histograms of Figure 15 capture both the temporal (with 1 day resolution) and spatial (with 1° resolution) variability of each regime's precipitation. The histograms make immediately obvious that CR1 has the widest precipitation histogram of all regimes, with substantial occurrences of values at the high end of precipitation range ($>$20 mm/d) that are virtually never encountered in other CRs. The next widest histograms are those by CR3 and CR2. We also plot in Figure 15 cumulative histogram curves in order to facilitate quick extraction of the fraction of occurrences higher or lower than certain precipitation rates or the precipitation rates of specific cumulative fractions of occurrence (e.g., the median precipitation rate, as a special case). By construction, the steeper the rise of the cumulative histogram curve, the smaller the fraction of gridcells with high daily precipitation rates. There is an abrupt change in this slope from CR5 to CR6, with the shape of the curve for the latter regime being very close to that for regimes CR7-9 and to a lesser extent CR10. Based on the cumulative frequency curves, the CRs can be grouped into four "precipitation regimes": CR1, CR2 and CR3, CR4, CR5, and CR10, and CR6-9.

Each of the panels of Figure 15 also includes information that summarizes the global apportionment of GPCP surface precipitation by MODIS CR. Similar to CRE, we are interested in the mean precipitation of each regime obtained by averaging the daily precipitation values (including zero precipitation) on the day and location of a regime's occurrence, as well as in the contribution of each CR to the global precipitation budget. As expected, the summary numerical values of Figure 15 indicate a general, albeit imperfect, correspondence with the mean CR cloud optical thicknesses of Figure 3. CR1's mean surface precipitation rate dwarfs all others, being about double than the second strongest precipitation producer, CR3. Despite occurring in only 6% of gridcells, CR1 contributes about 22% to the overall precipitation. Our regime indexing scheme (which was completely blind to precipitation) results in the first three regimes having also the highest precipitation rates and collectively contributing ~47% to the global total precipitation. Individually, the largest contribution (~28%) comes from the most frequent regime, CR10, despite its small mean cloud fraction CF_s or CF_m, mean precipitation rate, and the fact that it appears frequently to be not precipitating at all. The weakest rainfall, in terms of both mean rate and contribution, is found for CR6-9, with small RFOs and combinations of modest optical thicknesses and cloud fractions.

As with CRE, the seasonal variation of each regime's global mean precipitation is miniscule: the standard deviation of the 12 multiannual monthly means never exceeds 0.089 mm/d. The day-to-day and gridcell-to-gridcell variation of each regimes' annual precipitation, as expressed by the standard deviation of all available gridcell values ("STD" in Figure 15) can be, on the other hand, quite large. Given their small mean precipitation rates, CR6-10 feature surprisingly large precipitation variability, with a standard deviation 2–3 times greater than the mean. The greatest variability is exhibited by CR10, the most frequent and spatially expansive regime, with a fairly wide distribution of cloud fractions and very large zonal variations of precipitation (not shown). The results of Figure 15 indicate that individual regimes can potentially produce a very broad range of precipitation rates and also imply that geographic location (i.e., local environmental conditions) is a major

contributing factor to the precipitation efficiency of cloud mixtures that appear to share similar height-extinction covariations. This is another way of saying that similarity in these covariations as expressed by the joint histograms does not translate to trivial within-CR internal variability.

4.7. Radiative Versus Latent Heating by Regime

The energetic imprint on the atmosphere of the combined radiative and precipitative behavior of MODIS CRs can be illuminated by plotting CR mean precipitation converted to energy flux units W m^{-2} (mm/d multiplied by 28.95) [see, for example, *Trenberth et al.*, 2009] against the CRE of the net flux divergence, namely,

$$CRE_{ATM}^{net} = CRE_{TOA}^{net} - CRE_{SFC}^{net} = \left(CRE_{TOA}^{LW} + CRE_{TOA}^{SW}\right) - \left(CRE_{SFC}^{LW} + CRE_{SFC}^{SW}\right) \tag{2}$$

as shown in Figure 16. Because $CRE_{TOA}^{SW} \approx CRE_{SFC}^{SW}$, CRE_{ATM}^{net} is positive (indicating radiative heating of the atmosphere) for the CRs for which $CRE_{TOA}^{LW} > CRE_{SFC}^{LW}$ in Figure 14, i.e., those below the diagonal, and vice versa. Figure 16 makes immediately apparent that CRs warming the atmosphere radiatively also produce the largest implicit latent heat warming (CR1–3, and to a lesser extent CR4). On the other hand, the CRs that cool the atmosphere radiatively, CR6-9, also produce weak implicit latent heat warming. Apparently, cloud mixture decomposition by MODIS CR is successful in revealing clearly that clouds organize at global scales in such a way as to induce energy flow tendencies from areas where CRs dominated by high and midlevel clouds of higher precipitation rates are more prominent to areas where CRs dominated by low clouds of lower precipitation rates prevail. Furthermore, there is evidence that perturbations (anomalies) in individual CR radiative atmospheric warming or cooling are balanced by perturbations in their own latent heat release (via changes in precipitation) as described by *Lebsock et al.* [2010] who quantified such effects for their own oceanic tropical MODIS CRs.

5. Summary and Concluding Thoughts

An important step toward in-depth understanding of the role of clouds on the water and energy budget is a meaningful classification of the various cloud mixtures encountered in different parts of the globe at different times of the year. Cloud observations exist from many space-based observational platforms with a variety of remote sensing algorithms applied to both passive and active sensors. Passive observations have been available longer and have generally much better spatial coverage. In this, as well as in previous work, this class of observations was chosen for classifying and grouping mesoscale (i.e., ~1°) cloud mixtures into "weather states" or (as in this paper) "cloud regimes." Our cloud regime classification yielded 10 regimes for the globe as a whole and relied on a clustering algorithm applied to cloud optical thickness and cloud top pressure retrievals from measurements of the MODIS radiometer aboard the Terra and Aqua satellites. A multitude of other data sets was employed to investigate the nature of these cloud regimes beyond what can be gleaned from the passive observations alone. The essence of the analysis technique was to composite these complementary data sets as a function of MODIS cloud regime.

The two fundamental objectives of this work were as follows: (a) to examine aspects of the regimes' nature, including their morphological features and radiative and hydrological importance, as inferred from other coincident measurements; and (b) to identify the atmospheric conditions that tend to be associated with the regimes.

Our findings clearly indicate that the regimes obtained from joint histograms of cloud optical thickness and cloud top pressure have very disparate bulk cloud properties and vertical structure. They were distinctly separate in terms of dominant water phase (as measured by liquid/ice ratios in both cloud fractions and optical thickness), mean vertical location of their highest tops and lowest bases, vertical distribution of cloud fraction and water content, and number of overlapping cloud layers. When associated with traditional cloud type classifications made possible by active observations, their makeup also turned out to be very diverse and consistent with expectations based on interpretation of the passive observations, namely, the "mean" joint histogram representing each regime and the geographical distribution of their occurrences.

The MODIS cloud regimes were also found to form in environments characterized by distinct mesoscale vertical motions and temperature/relative humidity profiles. The regimes that tend to form in regions of ascent were also accompanied by warmer and more humid than average conditions in the lower and middle troposphere; these regimes were very often close to overcast and had a large proportion of high

clouds. On the other hand, the regimes forming in regions of weaker dynamical forcing (weaker ascent or even descent on average) were dominated by low clouds, were less likely to be overcast, and were associated with drier and cooler than average low to midtroposphere conditions.

We also applied our straightforward compositing approach on Clouds and the Earth's Radiant Energy System (CERES) and Global Precipitation Climatology Project (GPCP) daily data of the same 1° spatial resolution as that of the MODIS regimes for gridcells with identical Terra and Aqua regimes. The analysis revealed the CRs' distinct radiative and hydrological signatures. For example, even if some CRs had almost identical multiyear annual global means of one CRE component (SW or LW), they exhibited diverse values for the other component. Moreover, their contribution to the total global CRE was quite disparate because of strong dependencies on regime frequency of occurrence. CR distinctiveness according to this criterion (resemblance of mean values not translating to similarity in contributions) carried to precipitation as well.

No CR exhibited positive net global TOA CRE, although two (comprising different cloud types) had near-zero values. This is broadly consistent with previous analysis [*Hartmann et al.*, 1992; *Chen et al.*, 2000; *Oreopoulos and Rossow*, 2011] and the long-known fact that clouds tend to radiatively cool the planet. A comparison between surface and TOA LW CRE revealed a group of regimes with an atmospheric radiative warming bent (made of regimes with large proportions of high clouds), another group with a cooling predisposition (regimes with many low clouds), and two regimes with a near-neutral effect.

The three CRs that were the strongest precipitation producers, were found to be overall responsible for about half the total global precipitation as recorded by GPCP. These three CRs happened to also have the smallest assigned indices in our empirical regime ordering system which emphasized large total cloud fractions and strong cloud presence above the middle troposphere. We also showed that the histograms of precipitation varied greatly by CR and demonstrated unambiguously that the regimes with small precipitation means had very abrupt tails on the high end, indicative of a virtual absence of strong precipitation events (according to GPCP at least). Compared to the study of *Lee et al.* [2013] which, however, was restricted to the tropics only, we did not see as extreme a separation between precipitation-rich and precipitation-poor cloud regimes.

The concept of cloud regimes with the meaning assigned in the current work is now about 10 years old (it was first introduced by *Jakob and Tselioudis* [2003]). The ever-growing body of work built around it demonstrates its acceptance as a promising approach for making sense of a wide range of processes affecting and being affected by clouds. The present study serves as one more affirmation that cloud regimes derived from cluster analysis of passive satellite retrievals at O (100 km) are an appropriate foundation for decomposing the Earth's water and energy budget in a meaningful way. We advocate that this decomposition be replicated, with the aid of satellite simulators, to the best extent possible in GCMs as a means of identifying deficiencies and ultimately improving cloud representations.

References

Ackerman, S. A., K. I. Strabala, W. P. Menzel, R. A. Frey, C. Moeller, and L. E. Gumley (1998), Discriminating clear sky from clouds with MODIS, *J. Geophys. Res.*, *103*(D24), 32,141–32,157, doi:10.1029/1998JD200032.

Adler, R., C. Kidd, G. Petty, M. Morissey, and H. Goodman (2001), Intercomparison of global precipitation products: The third Precipitation Intercomparison Project (PIP-3), *Bull. Am. Meteorol. Soc.*, *82*, 1377–1396, doi:10.1175/1520-0477(2001)082<1377:IOGPPT>2.3.CO;2.

Adler, R., et al. (2003), The version-2 global precipitation climatology project (GPCP) monthly precipitation analysis (1979–present), *J. Hydrometeorol.*, *4*, 1147–1167, doi:10.1175/1525-7541(2003)004<1147:TVGPCP>2.0.CO;2.

Anderberg, M. R. (1973), *Cluster Analysis for Applications*, 359 pp., Elsevier, New York.

Chen, T., Y. Zhang, and W. Rossow (2000), Sensitivity of atmospheric radiative heating rate profiles to variations of cloud layer overlap, *J. Clim.*, *13*, 2941–2959, doi:10.1175/1520-0442(2000)013<2941:SOARHR>2.0.CO;2.

Gordon, N., and J. Norris (2010), Cluster analysis of midlatitude oceanic cloud regimes: Mean properties and temperature sensitivity, *Atmos. Chem. Phys.*, *10*, 6435–6459, doi:10.5194/acp-10-6435-2010.

Gryspeerdt, E., and P. Stier (2012), Regime-based analysis of aerosol-cloud interactions, *Geophys. Res. Lett.*, *39*, L21802, doi:10.1029/2012GL053221.

Gryspeerdt, E., P. Stier, and D. G. Partridge (2014), Satellite observations of cloud regime development: The role of aerosol processes, *Atmos. Chem. Phys.*, *14*, 1141–1158, doi:10.5194/acp-14-1141-2014.

Hartmann, D. L., M. E. Ockert-Bell, and M. L. Michelsen (1992), The effect of cloud type on Earth's energy balance: Global analysis, *J. Clim.*, *5*, 1281–1304, doi:10.1175/1520-0442(1992)005<1281:TEOCTO>2.0.CO;2.

Haynes, J., C. Jakob, W. Rossow, G. Tselioudis, and J. Brown (2011), Major characteristics of Southern Ocean cloud regimes and their effects on the energy budget, *J. Clim.*, *24*, 5061–5080, doi:10.1175/2011JCLI4052.1.

Jakob, C., and C. Schumacher (2008), Precipitation and latent heating characteristics of the major tropical western Pacific cloud regimes, *J. Clim.*, *21*, 4348–4364, doi:10.1175/2008JCLI2122.1.

Jakob, C., and G. Tselioudis (2003), Objective identification of cloud regimes in the tropical western Pacific, *Geophys. Res. Lett.*, *30*(21), 2082, doi:10.1029/2003GL018367.

Jakob, C., G. Tselioudis, and T. Hume (2005), The radiative, cloud, and thermodynamic properties of the major tropical western Pacific cloud regimes, *J. Clim.*, *18*, 1203–1215, doi:10.1175/JCLI3326.1.

Kato, S., S. Sun-Mack, W. F. Miller, F. G. Rose, Y. Chen, P. Minnis, and B. A. Wielicki (2010), Relationships among cloud occurrence frequency, overlap, and effective thickness derived from CALIPSO and CloudSat merged cloud vertical profiles, *J. Geophys. Res.*, *115*, D00H28, doi:10.1029/2009JD012277.

Kato, S., et al. (2011), Improvements of top-of-atmosphere and surface irradiance computations with CALIPSO, CloudSat, and MODIS derived cloud and aerosol properties, *J. Geophys. Res.*, *116*, D19209, doi:10.1029/2011JD16050.

Lebsock, M., C. Kummerow, and G. Stephens (2010), An observed tropical oceanic radiative-convective cloud feedback, *J. Clim.*, *23*, 2065–2078, doi:10.1175/2009JCLI3091.1.

Lee, D., L. Oreopoulos, G. Huffman, W. Rossow, and I. Kang (2013), The precipitation characteristics of ISCCP tropical weather states, *J. Clim.*, *26*, 772–788, doi:10.1175/JCLI-D-11-00718.1.

Marchand, R., T. Ackerman, M. Smyth, and W. B. Rossow (2010), A review of cloud top height and optical depth histograms from MISR, ISCCP, and MODIS, *J. Geophys. Res.*, *115*, D16206, doi:10.1029/2009JD013422.

Minnis, P., W. L. Smith, Jr., D. P. Garber, J. K. Ayers, D. R. Doelling (1994), Cloud properties derived from GOES-7 for Spring 1994 ARM Intensive Observing Period using version 1.0.0 of ARM satellite data analysis program, *NASA Reference Publication 1366*.

Minnis, P., et al. (2011), CERES Edition-2 cloud property retrievals using TRMM VIRS and Terra and Aqua MODIS data, Part I: Algorithms, *IEEE Trans. Geosci. Remote Sens.*, *49*, 4374–4400, doi:10.1109/TGRS.2011.2144601.

Oreopoulos, L., and W. Rossow (2011), The cloud radiative effects of International Satellite Cloud Climatology Project weather states, *J. Geophys. Res.*, *116*, D12202, doi:10.1029/2010JD015472.

Pincus, R., S. Platnick, S. Ackerman, R. Hemler, and R. Hofmann (2012), Reconciling simulated and observed views of clouds: MODIS, ISCCP, and the limits of instrument simulators, *J. Clim.*, *25*, 4699–4720, doi:10.1175/JCLI-D-11-00267.1.

Rienecker, M., et al. (2011), MERRA: NASA's Modern-Era Retrospective Analysis for research and applications, *J. Clim.*, *24*, 3624–3648, doi:10.1175/JCLI-D-11-00015.1.

Rossow, W., G. Tselioudis, A. Polak, and C. Jakob (2005), Tropical climate described as a distribution of weather states indicated by distinct mesoscale cloud property mixtures, *Geophys. Res. Lett.*, *32*, L21812, doi:10.1029/2005GL024584.

Rossow, W., A. Mekonnen, C. Pearl, and W. Goncalves (2013), Tropical precipitation extremes, *J. Clim.*, *26*, 1457–1466, doi:10.1175/JCLI-D-11-00725.1.

Sassen, K., and Z. Wang (2008), Classifying clouds around the globe with the CloudSat radar: 1-year of results, *Geophys. Res. Lett.*, *35*, L04805, doi:10.1029/2007GL032591.

Tan, J., and C. Jakob (2013), A three-hourly data set of the state of tropical convection based on cloud regimes, *Geophys. Res. Lett.*, *40*, 1415–1419, doi:10.1002/grl.50294.

Tian, B., E. Fetzer, B. Kahn, J. Teixeira, E. Manning, and T. Hearty (2013), Evaluating CMIP5 models using AIRS tropospheric air temperature and specific humidity climatology, *J. Geophys. Res. Atmos.*, *118*, 114–134, doi:10.1029/2012JD018607.

Trenberth, K. E., J. T. Fasullo, and J. Kiehl (2009), Earth's global energy budget, *Bull. Am. Meteorol. Soc.*, *90*, 311–323, doi:10.1175/2008BAMS2634.1.

Tselioudis, G., W. Rossow, Y. Zhang, and D. Konsta (2013), Global weather states and their properties from passive and active satellite cloud retrievals, *J. Clim.*, *26*, 7734–7746, doi:10.1175/JCLI-D-13-00024.1.

Williams, K., and G. Tselioudis (2007), GCM intercomparison of global cloud regimes: Present-day evaluation and climate change response, *Clim. Dyn.*, *29*, 231–250, doi:10.1007/s00382-007-0232-2.

Williams, K., and M. Webb (2009), A quantitative performance assessment of cloud regimes in climate models, *Clim. Dyn.*, *33*, 141–157, doi:10.1007/s00382-008-0443-1.

Yin, X., A. Gruber, and P. Arkin (2004), Comparison of the GPCP and CMAP merged gauge-satellite monthly precipitation products for the period 1979–2001, *J. Hydrometeorol.*, *5*, 1207–1222, doi:10.1175/JHM-392.1.

Zhang, Y., S. Klein, G. Mace, and J. Boyle (2007), Cluster analysis of tropical clouds using CloudSat data, *Geophys. Res. Lett.*, *34*, L12813, doi:10.1029/2007GL029336.